Biosensors and Bioelectronics: X 14 (2023) 100333

Contents lists available at ScienceDirect

Biosensors and Bioelectronics: X

journal homepage: www.journals.elsevier.com/biosensors-and-bioelectronics-x

Dynamic dielectrophoretic cell manipulation is enabled by an innovative electronics platform

Lourdes Albina Nirupa Julius, Henrik Scheidt, Gowri Krishnan, Moritz Becker, Omar Nassar, Sarai M. Torres-Delgado, Dario Mager, Vlad Badilita, Jan G. Korvink *

Institute of Microstructure Technology, Karlsruhe Institute of Technology, Hermann-von-Helmholtz-Platz 1, Eggenstein-Leopoldshafen, 76344, Germany

ARTICLE INFO

Keywords:
Dielectrophoresis
Cell/bacterium manipulation
Arbitrary path control
Deep learning

ABSTRACT

We report on a portable dielectrophoresis manipulation platform, for the positioning and immobilization of small dielectric objects, such as cells or microbes, using a circular array of up to six symmetrically arranged and independently controllable micro-electrodes. The system's micro-controller-instructed electronic drivers can be operated in three distinct modes. We demonstrate the system's function by actuating bacterial cells to specific locations and orientations within a region of interest. Using a deep learning approach, we map voltage phase combinations of the six electrodes to geometrical trap position locations, thereby facilitating smooth trajectory planning.

1. Introduction

H. Pohl et al. performed the first biological cell separation experiment using dielectrophoresis (DEP) in 1966 (Pohl and Hawk, 1966). Since then, it has become an indispensable tool to manipulate nano and micron-sized biotic and abiotic particles in the fields of biotechnology, medical diagnostics, and physics. Reducing the physical dimensions at which the electric forces operate, enhances their effect, and also eases their integration into lab-on-a-chip (LOC) and other micro total analysis systems (μTAS). Currently, DEP is one of the major building blocks contributing to single cell handling in microfluidics. Compared to other techniques used in handling single cells, such as hydrodynamics, acoustics, mechanics, and optics, the electrical methods show a better selectivity. Moreover, due to its dependence on the cell's intrinsic dielectric properties, DEP is a more straightforward technique because it does not require additional steps, such as labeling, as required by fluorescent and magnetic methods.

Electrokinetic movement of particles can be achieved using DC or AC power, and by adjusting the amplitude, frequency, and phase of signals applied at individual electrodes, different control modes of cell kinematics can be realized. These modes include electrophoresis, dielectrophoresis (DEP), electrorotation, and electrowetting. Electrophoresis is most commonly used for the separation of charged particles, such as DNA, RNA, and proteins, in the presence of a uniform electric field, by the application of a DC voltage across a pair of electrodes. In DEP, a polarizable particle in the presence of a uniform electric field aligns itself in the direction of the applied field due to an induced electrostatic dipole, but the particle does not undergo any migration. To achieve a lateral movement of the particle, a non-uniform field is essential to create a net force (Çetin and Li, 2011). DEP is widely used isolating and concentrating target cells and/or particles from a mixed population. Other applications include the hybridization of multiple protoplasts through electrofusion (Halfmann et al., 1983; Yang et al., 2010). Electro-rotation is used to extract the dielectric properties of particles and/or objects based on the angular velocity of the particle at different frequencies of the applied field (Huang et al., 2019; Trainito et al., 2019).

The voltages and frequencies used in DEP depend on whether the process is electrode-based DEP (eDEP), or insulator-based DEP (iDEP). The typical voltages used in eDEP are ranging from zero to tens of volts, while iDEP is mostly operated at higher voltage ranges of 100 s of Volts. The typical frequency ranges are from DC to 10 MHz, although there are groups reporting frequencies up to 50 MHz, for better separation of different types of cell lines (Manczak et al., 2018; Ramirez-Murillo et al., 2021). Park et al. (2009) used PCB-based electrodes that were separated from the cell suspension using glass. This prevented contamination of the electrodes and ensured the reuse of the PCB. Due to this non-contact mode of measurement (as can be expected for any iDEP) this approach required a high voltage supply (V_{pp} of 76 V at a frequency of 1 MHz) for its operation.

Biochips using electric forces are attractive due to their ease of manufacture using standard micro-fabrication processes. They are used for the precise positioning of cells, and allow reversible cell capture

* Corresponding author.
E-mail address: jan.korvink@kit.edu (J.G. Korvink).

https://doi.org/10.1016/j.biosx.2023.100333
Received 30 September 2022; Received in revised form 26 February 2023; Accepted 12 March 2023
Available online 16 March 2023

and release (Han et al., 2013). The huge majority of such biochips use relatively simple electrode systems (mostly two or four electrodes). Additionally, researchers have exploited micro-fabrication opportunities to develop novel electrode geometries such as sharp electrode tips, traps, and a combination of field lines and flow streamlines (Zhang et al., 2019). However, the reports on off-chip components including pumps, fluidic interconnects, and electronic control remain at a rudimentary level. For instance, most of the work on DEP reported in the literature relied on off-the-shelf signal generators to excite the electrodes on the biochips. Although they are beneficial for rapid testing, the number of output channels in standard signal generators is limited to two, and hence the experimental setup becomes bulky when the number of electrodes is increased.

Some of the reports on improving the electronics include complex CMOS circuits, or present application-specific electronics, thus with limited generality. Hunt et al. fabricated a CMOS integrated circuit and demonstrated trapping and droplet manipulation by controlling 128 × 256 pixels individually by applying voltages and frequencies in the range of 3 V to 5 V and 0 MHz to 1.8 MHz respectively (Hunt et al., 2008; Issadore et al., 2010). Although such an integrated circuit offers flexibility in the programmable control of the electrodes, it lacks flexibility at integrating novel electrode designs required for custom applications (Manaresi et al., 2003). It is also not a cost-effective solution and cannot be manufactured in an average laboratory. In other previously reported attempts of custom electronics, the source signal was nevertheless powered by a function generator, and the custom electronics was employed only for downstream processing, thereby requiring two setups, one for signal generation, and the other for signal processing (Braschler et al., 2008; Burgarella et al., 2013; RoyChaudhuri et al., 2011). Other handheld electronic systems were limited by the application or the range of applied voltages and frequencies (Jen and Chang, 2011; Qiao et al., 2011; Samanta et al., 2013). Jen and Chang (2011) have built a hand-held rare cell enrichment device, which operated at a V_{pp} of 16 V at 600 kHz, generated by using a voltage-to-frequency converter. This enrichment device used up to eight concentric electrodes which were sequentially activated with the 600 kHz signal using a micro-controller, and relays connected to each electrode. Samanta et al. (2013) reported a DEP-based impedance sensor to detect bacteria. In this device they generated the discrete frequencies in the range of 100 Hz to 100 kHz using a high-Q band-pass filter acting on a rectangular wave generated using an ATMEGA8 micro-controller. There have been attempts to demonstrate bead trapping in a micro-well array using a potential of 3.3 V, which was wirelessly powered using an RFID reader (Qiao et al., 2011). These examples show that reports on electronics for DEP applications are restricted to operate at a single voltage and frequency, or have a selection of discrete frequencies. Recent DEP-related literature shows a clear increase in the number of applications that employ DEP (Sarno et al., 2021). This trend suggests that a reconfigurable electronics platform can aid not just the dielectrophoresis community, but also attract new users across disciplines to the DEP community. A toolkit similar to the eLoad platform for the centrifugal microfluidics community (Delgado et al., 2018), by bringing along an extensive electrical tool box, and simplifying its use by requiring little programming and electrical hardware skills, would be greatly beneficial.

In this report we introduce an *Adaptable Dielectrophoresis Embedded Platform Tool* (ADEPT) which is a portable signal-generating electronic toolbox aiming at DEP applications. The work bridges the gap between application scientists (e.g., biologists, chemists, physicists) and electrical engineers by introducing a portable, versatile, and universal signal generating electronic toolbox, built using standard off-the-shelf electronic components. ADEPT can be applied to any application-defined micro-electrode design, and is able to configure the desired electrical output by activating micro-electrodes in different electrokinetic modes, thus achieving advanced control with high usability from the electronics point of view.

The Materials and methods section introduces the electronics design along with control software, the tools for electric field and trapping position simulation, the deep learning algorithm for non-linear interpolation of the position mapping, the fabrication process of the chip with electrodes arranged in a circular configuration, and the cell sample preparation and experimental setup. The Results and discussion section presents a thorough characterization of the electronics, the field simulation, and the cell manipulation experimental results. ADEPT is configured to offer programmable control of the voltage level, and the frequency and the relative phase applied independently to six individual electrodes. The V_p voltage can be varied from 0 V to 12 V and the frequency can vary from 0 MHz to 12 MHz. These ranges of operation are specific to the components selected for this project, which were considered a good trade off between flexibility of operation, complexity of external circuitry and programming required, accessibility and price. Nonetheless, these values can be of course further extended with a different choice of components and hence do not pose a fundamental limitation. The combination of voltages that need to be applied to the electrodes to position the particle at a desired location in the field of view can be reasonably predicted using finite element field simulations, and more efficiently using deep learning. The circular configuration of the electrodes, and the high flexibility in parameter selection, opens up a plethora of manipulation possibilities such as positioning, manipulation, rotation around a desired axis, as well as particle concentration in a user-defined trap position.

2. Materials and methods

2.1. Electronics design

The flexible signal generation circuit presented in this work was developed as a one-stop-shop electronics solution for eDEP applications. The capabilities of the ADEPT unit were demonstrated using a microfluidic chip, fabricated in-house, possessing six electrodes, as reported in Section 2.5. The electronic design and layout files of ADEPT hardware along with the software files can be found at the github link: https://github.com/on6315/ADEPT_DEP_Module.git.The signal generator unit consists of four different modules, (I) a power supply, (II) a signal generation unit, (III) a switching unit, and (IV) a controller. Fig. 1 illustrates the schematic configurations of the board, which is powered using an off-the-shelf DC power adapter delivering 12 V and 3 A.

Module I. The board's power supply module possesses voltage regulators to provide the ±12 V and +5 V required for driving the operational amplifiers ICs (opamps) included on the board. Also, a voltage regulator is supplemented to provide the +1.8 V for powering the reference clock and the direct digital synthesizer (DDS) (AD9913, Analog Devices) ICs.

Module II. The signal generation module consists of six different channels to individually control the signal provided to each of the six electrodes integrated into the microfluidic chip. Each channel generates four different modes of voltage signals: (i) a ground signal, (ii) a DC signal ranging from 0 V to 5 V, (iii) an AC signal with a variable V_{pp} amplitude amplification of 1 V to 10 V, and frequencies from 0 MHz to 10 MHz in steps of 0.058 Hz, and a relative phase shift from 0 to 2 π with steps of 0.0001 rad, and (iv) a summation of two AC signals with controllable amplitudes, frequencies and relative phase shifts with the same ranges mentioned for the third mode (see *Operation modes* below).

Module III. The switching module serves as the board's output ports connected to the electrodes on the microfluidic chip. This module includes six analog 4 × 1 multiplexers (MAX14753EUE+, Maxim Integrated) to excite each electrode with one of the four modes mentioned earlier. The chosen multiplexer is capable of operating at +5 V on the digital port and up to ±36 V on the analog port. The multiplexer is powered with ±12 V to provide signals with amplitudes up to ±10 V. AC signals with frequencies of up to 30 MHz are supported.

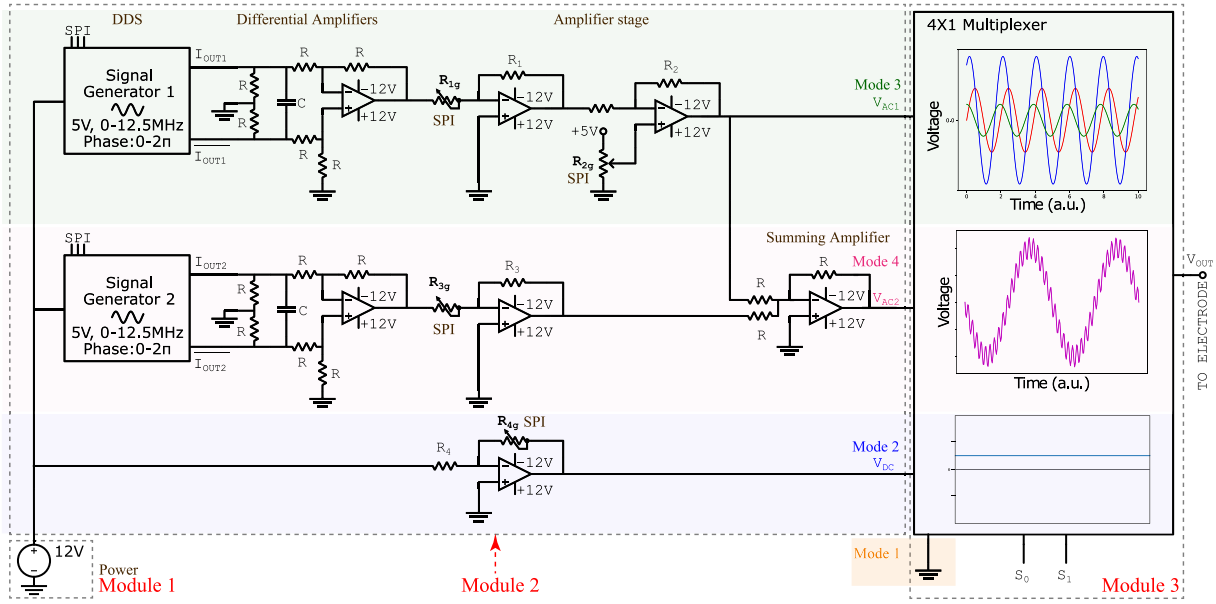

Fig. 1. Schematic diagram of the DEP electronics of a single channel to control a single electrode integrated onto the microfluidic chip.

Module IV. The control module uses an Arduino Mega 2560 Microcontroller Unit (MCU). The MCU is used to: (i) define the generated signal by programming the direct digital synthesizers (DDS) communicated through the Serial Peripheral Interface (SPI), (ii) set signal amplitudes and offsets by programming a network of digital potentiometers also via SPI, and (iii) select the output modes by addressing the multiplexers' selection pins with digital outputs of the micro-controller.

Operation modes. Now we explain the four different modes generated by the board in detail. In the first mode, a ground signal is directly coupled to the output port through the multiplexer. In the second mode, the amplitude of the DC signal is determined using a high precision operational amplifier (OPA4277, Texas Instruments) in an inverting amplifier configuration. The amplifier is supplied with a −12 V signal, and a 100 kΩ variable digital potentiometer (AD8400, Analog Devices) is used as the feedback resistor to vary the amplifier's gain and consequently achieve a variable amplitude in the range of 0.6 V to 10 V. In the third and fourth mode, the DDS is utilized to generate the AC signals. The DDS output signal's frequency f_{out} is adjustable in the range of 0 to 100 MHz with a resolution of 32 bits, while the phase is set with a resolution of 14 bits. DDS ICs produce the output frequency by accumulating phases in steps of the frequency tuning word (FTW) at each clock pulse. The output frequency can be calculated by $f_{\text{out}} = f_c \cdot \text{FTW} \cdot 2^{-32}$, where f_c is the frequency of the clock. The reference clock (511JBA250M000BAG, Skyworks Solutions Inc.) provides $f_c = 250$ MHz in the low-voltage differential signaling (LVDS) standard to the DDS ICs. The phase data is then translated to amplitude data through a lookup table. The final stage of the DDS IC is a digital-to-analog-converter (DAC) that generates complementary current output ranging from 0 mA to 4.6 mA. Determined with 50 Ω, the output signal ranges over 0 V to 0.23 V.

To apply an offset to the generated AC signal, a differential amplifier circuit is used to pre-amplify the signal with a fixed factor of 4, which raises the V_{pp} amplitude of the output signal to 0.9 V. The amplifier used in this circuit is the high-speed, low power, low distortion voltage feedback Operational Amplifier LM6171AIM from Texas Instruments, with a unity-gain-bandwidth of 100 MHz and a supported output range up to ±18 V. Thus, the chosen amplifier can boost signals up to 10 MHz. The output signal is then passed to an inverting amplifier circuit using the same operational amplifier (LM6171AIM) with a 1 kΩ digital potentiometer (AD8400, Analog Devices) to amplify the AC signal with a gain $A \in (1, 20)$. A second inverting amplifier stage follows, to introduce offset in the amplified sinusoidal signal that is controlled by another digital potentiometer through the SPI interface.

In the fourth mode, the DDSs acts as a sinusoidal source signal with adjustable frequency and phase, similar to the signal of the third option. Also, the following differential amplifier circuit and the inverting amplifier circuit to control the amplitude are set up similarly to the third mode for the introduction of an offset. The generated signal, and the signal from the third mode, are then added up using a summing amplifier circuit (opamp LM6171AIM, ±12 V power supply) to generate the output signal used for the fourth option. The transfer functions of the last three operational modes are described by the following equations:

Voltage V_{DC}:

$$V_{DC}(R_{4g}) = \frac{R_{4g}}{R_4} \cdot (12\ \text{V}), \tag{1}$$

Voltage V_{AC1}:

$$V_{\text{AC1}}(f_1, \varphi_1, R_{1g}, R_{2g}) = \frac{R_1}{R_{1g}} \cdot V_{\text{ACin1}}(f_1, \varphi_1) + 2 \cdot \frac{R_{2g}}{10^5 \Omega - R_{2g}} \cdot (5\ \text{V}), \tag{2}$$

Voltage V_{AC2}:

$$V_{AC2}(f_1, f_2, \varphi_1, \varphi_2, R_{1g}, R_{2g}, R_{3g}) = -\frac{R_3}{R_{3g}} \cdot V_{ACin2}(f_2, \varphi_2) + V_{AC1}(f_1, \varphi_1). \tag{3}$$

2.2. Coding

The software to control the amplitude, frequency, phase, offset, and the selection of the modes for each of the six electrodes consists of three parts: (i) Graphical User Interface (GUI), (ii) Arduino control, and (iii) back end C++ class file. The front end GUI (as seen in Fig. 2b or Fig. 6c) is written in Python and communicates with the Arduino over a serial port with a baud rate of 9600. The user can input phase combinations or send a random phase pattern along with the desired frequency and amplitude. Additionally, buttons to select different operations, such as an electro-rotation, trapping the particle/cell in the center, and apply a push-pull effect, are achieved by switching the frequency in the nDEP/pDEP regime. The GUI also allows the user to draw, using the mouse, an arbitrary path on a canvas that a particle or cell should trace. Each location on the canvas is mapped to a phase combination

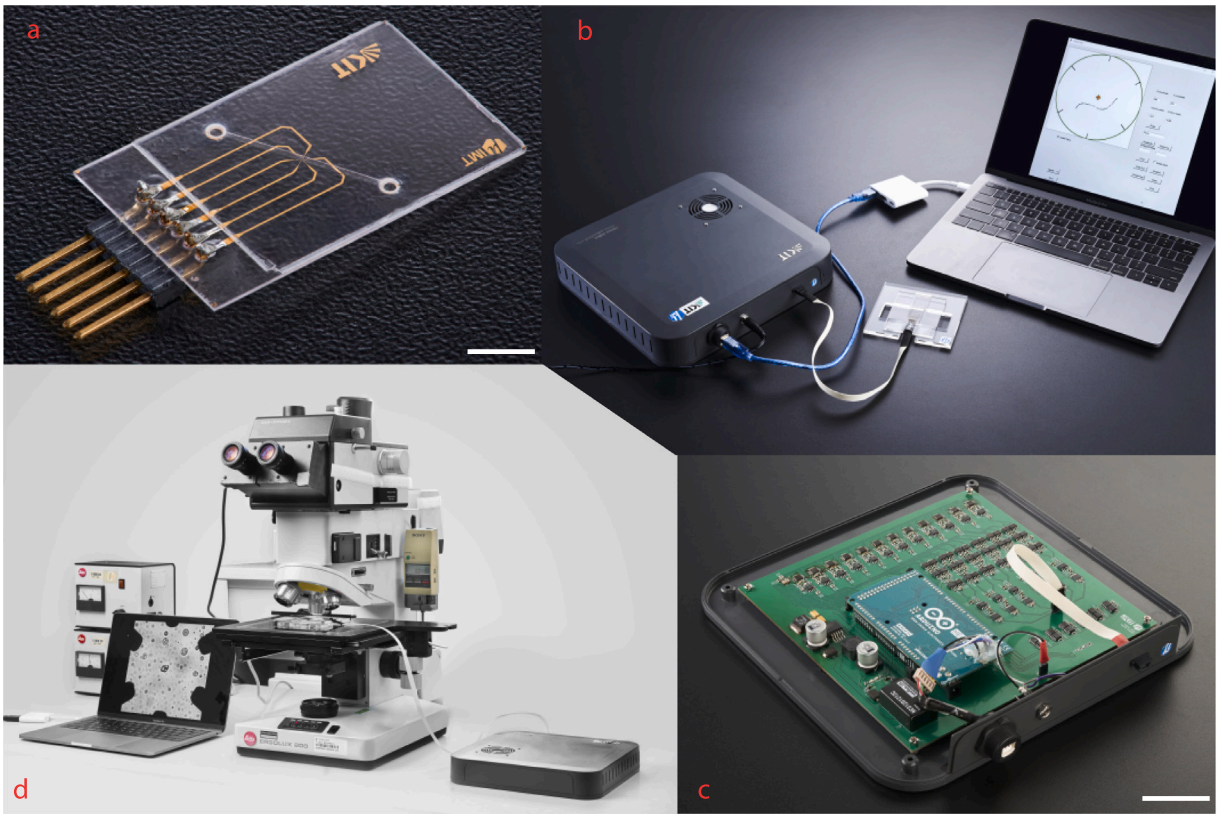

Fig. 2. *ADEPT* platform. (a) An electrode array is defined by UV photolithography on a microfluidic glass chip, featuring two fluidic ports, and a six-electrode interfacing pin connector. The scale bar length is 5 mm. (b) The chip, mounted on a transparent polymer platform, is wired to a micro-controller, which in turn connects via USB to a portable computer with a graphical user interface. (c) The micro-controller embeds an Arduino platform and individual power management circuit drivers for the electrodes. The scale bar length is 5 cm. (d) The chip platform conveniently slides into the optical path of a microscope to facilitate visual observation of the cell manipulation.

obtained through simulation, and verified experimentally. A click on any location on the GUI canvas would also take the particle or cell to the corresponding location on the microfluidic chip. The Arduino is programmed to receive data from the GUI and send the corresponding commands to the DEP electronic modules over SPI and through digital outputs. The Arduino code calls different functions from the C++ class to control the DDS (AD9913), the digital potentiometer (AD4800), and the multiplexer (MAX14753).

2.3. Simulations

Mathematica

An interactive electrostatic finite element method (FEM) simulation toolbox was written using NDSolve, a general numerical differential equation solver in Mathematica (Wolfram Research, Inc., 2021). Dirichlet boundary conditions for the voltages were applied at the sites of the six electrodes.

COMSOL

COMSOL Multiphysics® (COMSOL AB, Sweden) was used to perform FEM simulations to both estimate the electric field distribution (AC/DC Module), and to monitor the output positioning of a test particle (Particle Tracking Module). A six-electrode circular geometry was used for the time-domain simulations. The relative tolerances of the simulations were set to 1×10^{-5}. The electrodes were fed with time-varying sinusoidal voltages with a fixed maximum amplitude of 10 V, and a frequency of 100 Hz. The phase difference between the six electrodes determined the location of the particle trap.

Python simulation using COMSOL data

A COMSOL master file was generated to capture the electric field (E_x, E_y) in the trapping zone by exciting one electrode with a V_{pp} amplitude of 10 V at 100 Hz at the onset. This file was then used to compute the time varying field at each location in the trapping zone for each of the six electrodes. The phase shift corresponding to each electrode was also accounted for in the time varying field. The field patterns of the individual electrodes were rotated depending on their angle of rotation with respect to the first electrode. Finally, a superposition operation is performed on the six field patterns generated for each electrode independently for every time step, and the trap location is identified as the location with the weakest field within the trapping zone. This process of identifying the trap location was repeated for several random phase combinations for the six electrodes and the resulting trap positions were plotted using a Python Bokeh plot. The advantage of the Bokeh plot is that, as the mouse point hovers over the trapping zone in the plot, the phase combinations required are listed as seen in Fig. 4b.

2.4. Neural network model

We utilized a deep neural network (DNN) to approximate the cell position as a function of the electrodes' phases, as they seem to inhibit regions of both linear and non-linear correlations, which prevents the use of simpler interpolation techniques. As a tool, Deep Learning (DL) has demonstrated great success over various domains by end-to-end learning, i.e., an algorithm learns, given only an input and the target, to automatically detect correlations. DNNs are most commonly implemented as stacked layers of artificial neurons, where the weight of each neuron is updated (or learned) with backpropagation (Matias et al., 2014) and gradient descent, to minimize a loss function on given

training data. Regularization plays an important role to avoid overfitting of the NN, i.e., unwanted memorization of the training samples, and bad generalization, and commonly used approaches are batch normalization, dropout, and data augmentation. The usage of non-linear activation functions, such as the rectified linear unit (ReLU) (Nair and Hinton, 2010), with a sufficient number of processing layers (depth), allows neural networks to approximate any arbitrary function between inputs and targets. We refer to LeCun et al. (2015) for a more detailed description of the entire DL idea.

Problem definition in terms of DL: We defined our simulation dataset (from Section 3.2.) as $\mathcal{D} = \{(\mathbf{x}, \mathbf{y})_i\}_{i=1}^{|\mathcal{D}|}$, where $(\mathbf{x}, \mathbf{y})_i$ is a pair including the input $\mathbf{x} \in [0°, 360°]$ for n phases, and the associated target $\mathbf{y} \in [-50\,\mu m, 50\,\mu m]$ is given by the cell position (x, y). We considered a regression model $\mathrm{F}_{\theta}(\cdot)$, represented by a multi-layer perceptron (MLP) with parameters θ. The network parameters θ were learned in a supervised manner using the database $\mathcal{D}$ in order to minimize a loss function $\mathcal{L}$ (e.g., the mean squared error (MSE)) between the prediction $\hat{\mathbf{y}} = \mathrm{F}_{\theta}(\mathbf{x})$ and the target $\mathbf{y}$. Implementation was done in Python using the deep learning framework (`PyTorch`) (Paszke et al., 2019), and we utilized automated search algorithms to find the best hyperparameters and architecture properties using (`ray tune`) (Liaw et al., 2018), a framework that allows neural architecture search and automated hyperparameter optimization (HPO). We manually selected and fine tuned our architecture and parameters starting from the best configuration with respect to validation error given over 150 runs for different search spaces. Variables during HPO included the number of layers, neurons per layer, dropout, augmentation noise, different activation functions (including a periodic activation (Ziyin et al., 2020)), loss functions, varying optimizers with learning rates and weight decay, and the batch size. The data was augmented during training via rotation by multiples of 60°, and with additive uniform noise to both inputs and targets. Each layer of the neural network contained a block consisting of an fully-connected (FC) layer instance, the activation function, batch normalization and dropout.

2.5. DEP microfluidic chip fabrication

The microfluidic chip was designed to have six 30 μm wide electrodes arranged in a circular fashion enclosing an imaging area of 100 μm in diameter. A 500 μm thick 4-inch-wide MEMpax substrate was coated with a Cr/Au (20 nm/60 nm) seed layer and subsequently SU-8 photoresist was patterned on the wafer using UV-lithography (EVG®620 EV Group) to define the electrodes. The exposed pattern was electroplated with gold to a height of 5 μm and subsequently the SU-8 mold was stripped off using an R3T plasma etcher. Finally, the Cr/Au seed layer was etched out to form electrode patterns. The microfluidic channels were prepared by Xurography using a 75 μm thick double sided Pressure Sensitive Adhesive (PSA) tape. The knife-cutter (CraftRobo Pro, Graphtec, USA) was used to cut the 150 μm wide channels on the PSA. The inlet and outlet holes were cut on a 100 μm thick cover slip using a nanosecond laser (PIRANHA® ACSYS, Germany). The laser was also used to cut holes in the 500 μm thick 4-inch-wide MEMpax substrate to insert the pin headers after assembling the microfluidic chip. The glass layer with the electrodes, the PSA channel layer, and the coverslip were stacked through lamination. Finally, 6 × 1 pin headers were soldered to the assembled chip to connect the electrodes to the DEP electronics unit via cables. The fabricated chip is shown in Fig. 2a.

2.6. Sample preparation and experimental setup

Unicellular cyanobacteria of different species and shapes were used in the study. This included rod shaped *Thermosynechococcus elongatus* and spherical *Synechocystis sp. PCC 6803* cells. Additionally, yeast cells were also used in the study. The DEP buffer solution was made up of 10 mM TES buffer, 0.1 mM $CaCl_2$, and 236 mM sucrose at a pH value of 8. The cells were suspended in the DEP buffer solution. For the initial experiments, 5 μL of cell suspension was dispensed on the DEP chip and sealed with a cover slip. The chip and the cover slip assembly was then sealed with parafilm oil to prevent evaporation and the generation of air bubbles. The imaging was performed using a 40×/0.75 Nikon objective affixed to a Nikon Eclipse Microscope. The positional trapping experiments, after the application of different phase combinations, were performed on the DEP microchips with sealed channels. The imaging was performed using a Leitz (ERGOLUX 200) Microscope fitted with an iDS camera (model UI-3060CP-C-HQ R2, IDS Imaging Development Systems GmbH, Germany). The uEye Cockpit (IDS Imaging Development Systems GmbH, Germany) software was used to record the videos with a frame rate of 10.21 frames per second. The experimental setup, along with the assembled and packaged DEP electronics unit, is shown in Fig. 2b-d.

2.7. Image processing

A custom code was written in Python (Python Version 3.7.6 (Van Rossum and Drake, 2009)) to process the acquired videos. The image frames corresponding to the cells trapped in the initial central position and the final position based on the applied input phase combinations were processed. The images were converted to gray scale, a Gaussian blur was subsequently applied, followed by automatic image thresholding using Otsu's method (Bangare et al., 2015). In order to identify the center of the imaging area for each recorded experimental video, the tip of each electrode was found, and a circle was fit to these points. The center of the fitted circle was then taken as the origin of the position calculations of the trapped cell/particle. To identify only the electrodes in the image, an erosion operation was performed on the thresholded image, followed by area thresholding to eliminate the small objects in the image, including the cells. Then the closest points to the center of the image among the extreme points in each of the six electrodes were identified as the tips of each of the electrodes. The thresholded image before erosion was then applied with area thresholding to identify cell centroid positions. In order to compare the cell positions, given the same input phase combination, between the COMSOL simulation and the experimental results, the position of the cells/particles extracted from the experimental results were rotated to account for the electrodes' orientations that arose during the imaging process.

3. Results and discussion

3.1. Hardware characterization

The finalized printed circuit board is shown in Fig. 2c. The ADEPT-generated output signals were tested for different frequencies and load resistances and are reported in this section. The time response of the board was also examined when switching between different voltage levels. Fig. 3a demonstrates the transition in the peak to peak voltage (V_{pp}) as the frequency of the output signal increased from 10 Hz to 30 MHz at different amplification factors (A) of the operational amplifier, with the output port connected to an oscilloscope. As observed in Fig. 3a, the output voltage V_{pp} is constant for frequencies up to 2 MHz and at higher frequencies the output voltage drops due to the bandwidth of the opamp in use. ADEPT can operate over such a wide range of frequencies without a voltage drop, and despite the voltage drop of the signal beyond 2 MHz, ADEPT can function effectively up to a frequency of 12 MHz with a slight compromise on the moving speed of the particle to the desired trap location. For typical DEP applications, signals with frequencies ranging from 100 Hz to 10 MHz are required, and hence, the developed board can satisfy the requirements of DEP applications . The frequency spectrum of the signal was measured at the end of the amplifier stage. Fig. 3b shows a stacked y-axis plot of the output spectrum when ADEPT was programmed to synthesize different

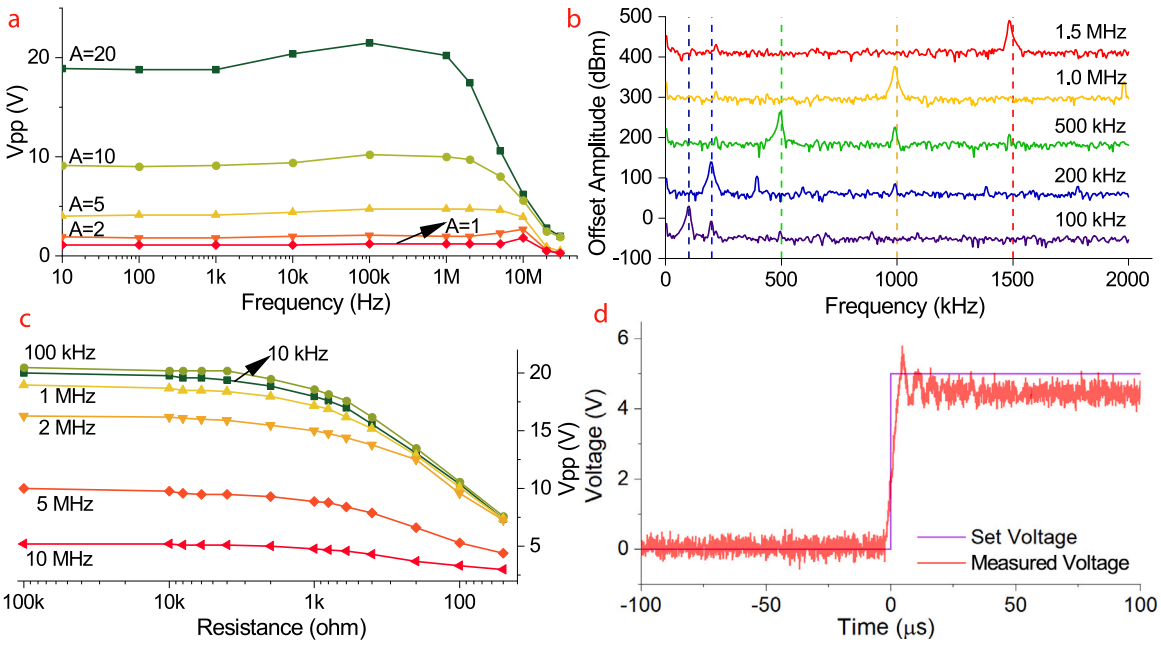

Fig. 3. Characterization plots of the DEP electronics unit. (a) The output peak-to-peak voltage (V_{pp}) of the developed board, versus frequency in the operating range from 10 Hz to 30 MHz, at different amplification factors (A). (b) Stacked plot of the frequency spectrum, from 100 kHz to 1.5 MHz, at the output of the differential pre-amplifier when the DDS chip was set to different frequencies to monitor for jitters. (c) The output voltage peak-to-peak amplitude at different load resistances connected to the board (1 kΩ–100 kΩ) for discrete frequencies in the range of 100 kHz to 10 MHz. (d) The measured settling curve of the output signal with the board operating in the DC mode. The output signal had a settling time of around a few 10 s of µs when the voltage changed between levels with a voltage difference of 5 V.

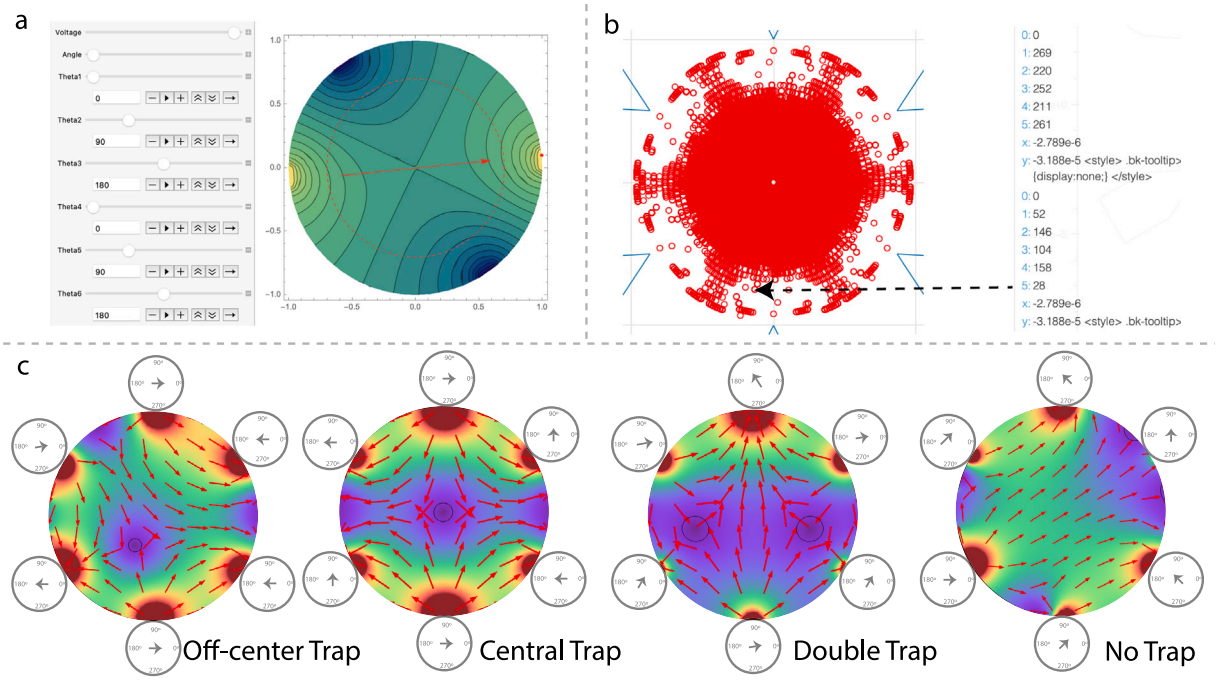

Fig. 4. (a) FEM based interactive toolbox coded using Mathematica. (b) Python based Bokeh plot which estimates trap locations using superposition on a single electrode field pattern obtained using COMSOL simulation. The various phase combinations to trap a cell at the location pointed out by the arrow is listed in the GUI. (c) Computed surface and arrow plots of the normalized electric field for phase combinations obtained by varying the phase of the electrodes in the range of 0° to 360°, using COMSOL. The black circle represents the particle trap location within the experimental field of view.

frequencies between 100 kHz to 1.5 MHz. The DC output signal switched between different values. Fig. 3d demonstrates the change measured using an oscilloscope when the output voltage changed from 0 V to 5 V. At voltage levels with a difference of 5 V, the output signal settled to its final value after a few tens of µs with an overshoot of 0.8 V.

Since the output signals were fed through the DEP buffer solution, which possessed a relatively high resistance in the range of a few kΩ, characterization on the effect of different load values was of great interest. Fig. 3c shows the output voltage obtained for different values of purely resistive loads connected to the board (1 Ω–100 kΩ). The

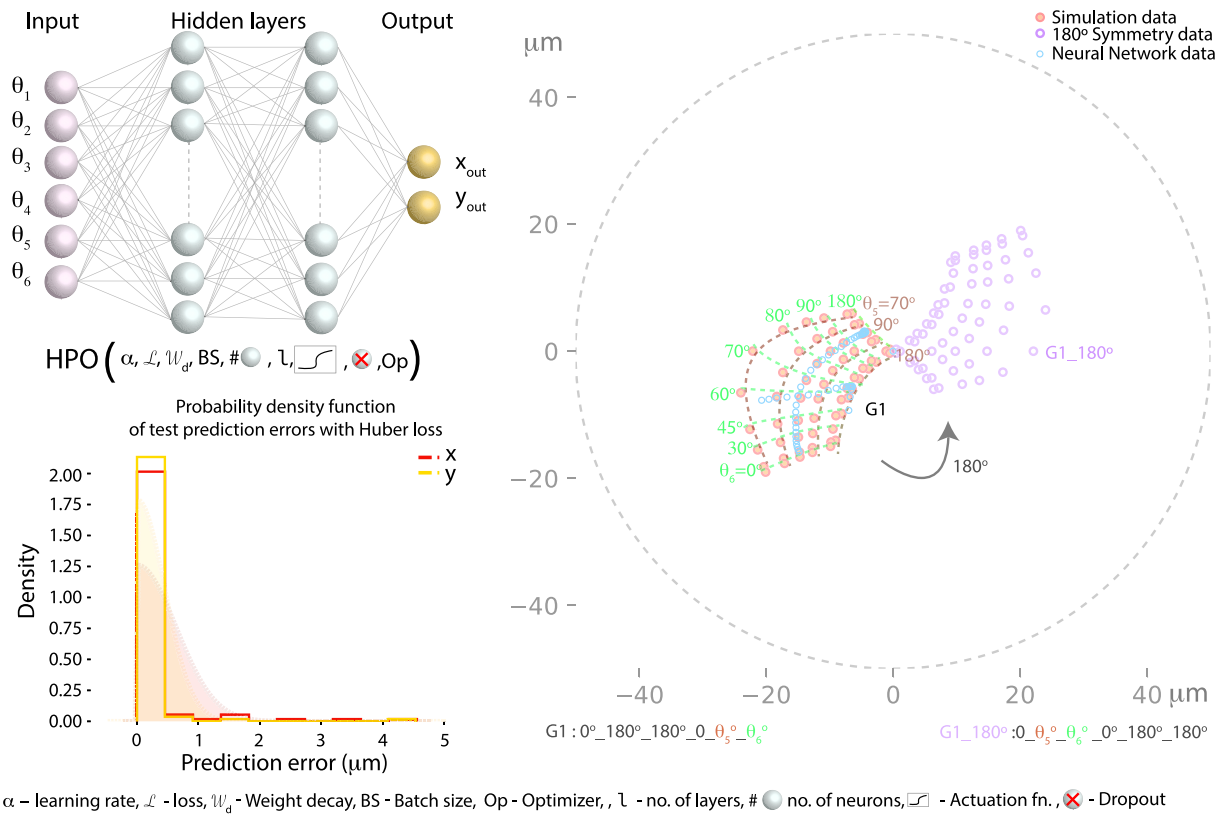

Fig. 5. (a) Schematic of the neural network map, listing the parameters used for hyperparameter optimization (HPO). (b) The probability density function of 122 test prediction errors with Huber loss of the neural network model. (c) COMSOL phase combination for the $G(5,6)$ family of curves, and location mapping after applying 180° rotational symmetry. The predictions of the neural network model are indicated by blue circles.

measurements were performed for discrete frequencies in the range of 100 kHz to 10 MHz. At high load resistances the amplitude of the output signal was relatively constant, but the voltage started to drop gradually as the resistance decreased, demanding more current/power from the system.

3.2. Simulation and deep learning

The trap location of the particle can be controlled in several ways: either by varying the combination of the phases applied to each of the six individual electrodes, or by controlling the magnitude of the applied voltages and the physical position of the electrodes. In the supplementary information (See Figure A1 and S4.gif), we demonstrate that the voltage magnitude and the electrode position can be also used for precise manipulation, which enables in principle the use of various electrode topologies, depending on the application. In the present work, we are using the phase combination for trap control. The frequency used for trapping the cells (200 kHz) is in the negative DEP regime for the cells and hence the cells experience a pull away from the electrodes. The trap location is the position were the superposition of the net electric field is minimum as shown in the simulations in Fig. 4a and Fig. 4c. The different simulation approaches used in this work presented in Section 2.3 are shown in Fig. 4. The FEM toolbox using Mathematica (Fig. 4a) served as a quick interactive guide to visualize the field pattern trends of the trap locations in a qualitative manner. Alternatively, the phase combinations could be selected from the Bokeh plot (Fig. 4b). The Bokeh plot was generated using a Python code that superposed the fields generated by the six electrodes. The input for the Python code was the field pattern generated by a single excited electrode computed using COMSOL. The Python code subsequently performed phase additions, generated a time dependent signal, performed rotation of the field pattern based on the electrode orientation, and finally identified the field minima after the superposition of the fields of the six electrodes. The trap location from the various minimum points over one period was identified as the location where the points were close together. As evident from the simulations shown in the Bokeh plot (Fig. 4b), the inner portion of the trapping region with radius less than 40 μm had the trap locations mapped to different phase combinations, and also, multiple phase combinations could have the same trap location. The outer regions of the Bokeh plot close to the electrodes showed lesser mapping due to the strong field emanating from an electrode.

Compared to the previous two simulation approaches, which provide a quick approximate solution to the trap location, the COMSOL time-dependent study with particle tracking feature (presented in Fig. 4c) offers more accurate prediction of the trap location. To provide guidelines to the user for the selection of the phases, in order to trap the particle/cell at the desired location, a trend map was generated as shown in Fig. 5c. Fig. 5c is the map of the pool of trap points obtained using simulations whose phase values are known. The number of permutations to select six phases from 360° (steps of 1°) is large ($\approx 2 \times 10^{+15}$) and would lead to multiple combinations of the phase resulting in the same x and y output points. The goal was to identify the phase combinations to obtain reliable traps in the complete trapping zone. Thus, to simplify the selection of the appropriate phase angles, we started by picking the initial trap points from the Bokeh and Mathematica tool box, and then vary the phase of certain electrodes to observe the change in the trap location. We report three families of curves (G(5,6) shown in Fig. 5c) as well as Figure A.2, and G(4,5) and G(4) as seen in Figure A.2 which sufficiently cover the approximately one-fourth of the 100 μm trapping zone. As the COMSOL simulations are slow and resource-intensive (roughly 30 min per data point), additional data points were included in the data pool by applying symmetry and interpolation using a neural network model to cover the entire trapping zone.

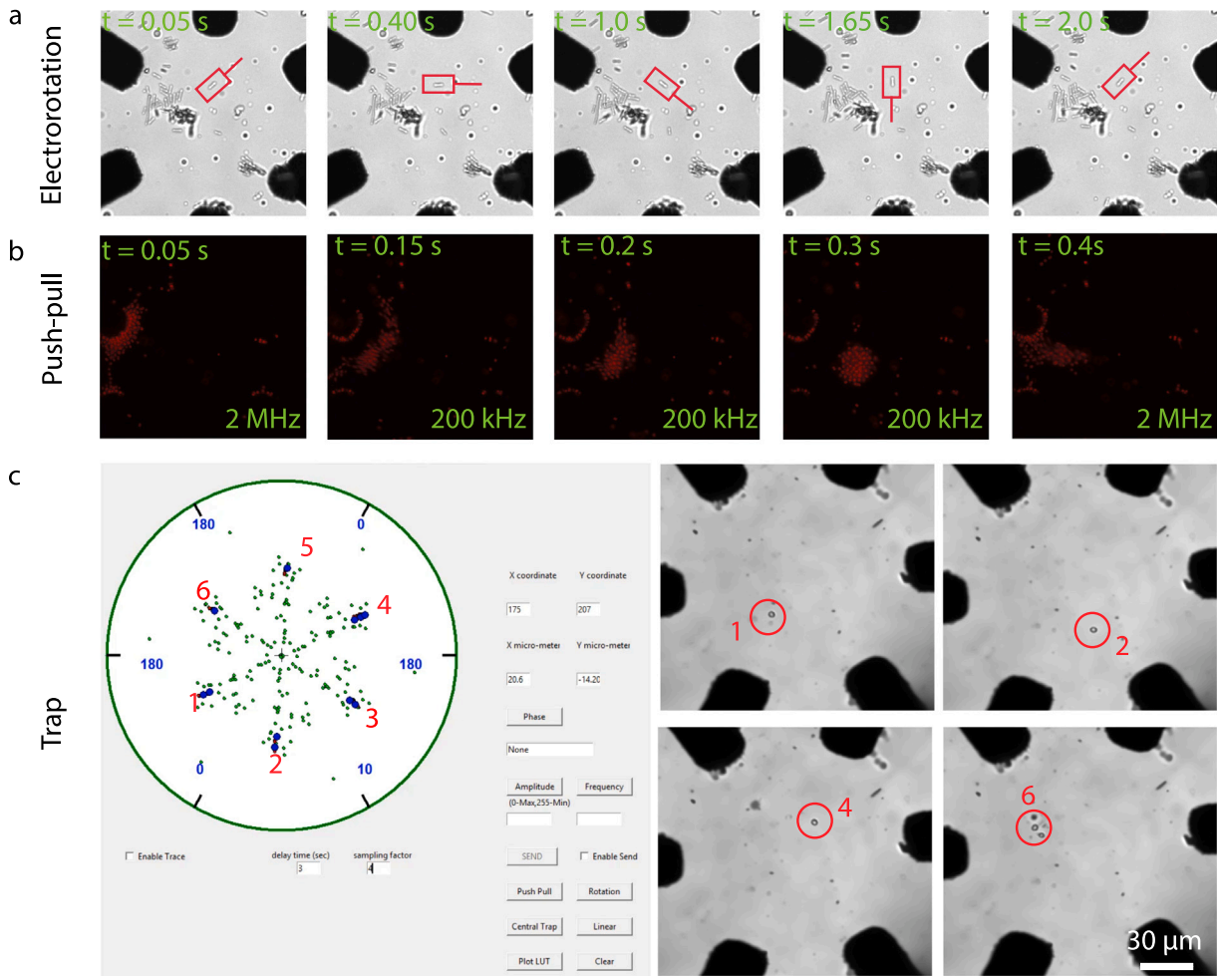

Fig. 6. Cell experiments: (a) Electrorotation. (b) Push–pull effect. (c) Positional trapping of bacteria at arbitrary trapping location as drawn on the canvas of the GUI by the user. The red contour shows the segmented cell whose position changes by changing the phase combination as indicated in the GUI. Voltage signals with an amplitude of 18 V_{pp}, and frequency 200 Hz, were applied to the six electrodes.

The first family of phase combinations is G(5,6) = (0°, 180°, 180°, 0°, θ_5, θ_6), fixing the phases of the first four electrodes. As θ_5 is varied from 70° to 180°, the trap points move outward from the center of the trapping zone, with an increasingly curved trajectory of points for the θ_6 values from 0° to 180°. The second set of phase combinations G(4,5) = (0°, 180°, 180°, θ_4, θ_5, 10°) is obtained by varying θ_4 and θ_5 from 0° to 70° and 60° to 180°, respectively. Increasing the θ_4 causes the trap location to move anti-clockwise, while increasing θ_5 to 180° moves the trap location closer to the center. The third set of phase combinations G(4) = (315°, 0°, 90°, θ_4, 90°, 0°), causes a straight line variation of the trap location as the phase of the fourth electrode is varied from 0° to 45°, outward from the center. The symmetrical arrangement of the six electrodes in a circular fashion offers the possibility to augment extra data points by performing rotation operations (five times) with a step of 60°. The plot in Fig. 5c shows the augmented data points after performing 180° rotation operation, while the rest of the data points are not shown in the plot.

In order to interpolate regions that are not identified by the time-costly simulation, the neural network model was developed as discussed in Section 2.4. After training on 969 simulated and augmented phase-position pairs, the model predicts the cell position given previously unseen electrode phases with a mean squared error of 0.27(106) µm (also shown in Fig. 5b). Since the model was not specifically regularized to reproduce our manually inferred patterns, but only to minimize the loss between input and targets of the training data, the network picked up the underlying concept. We show in Fig. 5c how interpolation of missing data points approximates the assumed patterns (linear or curved based on observation) of the different families of curves.

3.3. Cell experiments

The demonstration of various functionalities (i.e. electrorotation, push–pull effect, and positional trap) offered by the DEP platform are shown in Fig. 6. Electrorotation is widely used in label free single cell diagnosis of malignant cells based on a cell's membrane capacitance and/or their dielectric properties. The torque generated by the rotational electric field is proportional to the imaginary part of the Clausius–Mossotti (CM) factor. The dielectric constant and the conductivity of the bacterium were estimated from the electrorotation spectrum, which is the rotational speed as a function of the applied frequency. Fig. 6a shows the electrorotation of the rod-shaped *Thermosynechococcus elongatus* at various time stamps when a frequency of 100 kHz, and a 60° phase shift, was applied among the electrodes (see supplementary video S1). The push–pull effect on the cell was accomplished by trapping the cells with a particular location in the imaging field of view and switching the frequency of one of the electrodes between 200 kHz and 2 MHz. The switching of the bacteria from the trap location to the location close to the electrode took 0.3 s after the application of the frequency. Supplementary video (S2) of the push–pull experiments performed on spherical bacteria are provided. This video captures the autofluorescent cells in the CY3 (Cyanine-3) microscope fluorescence channel.

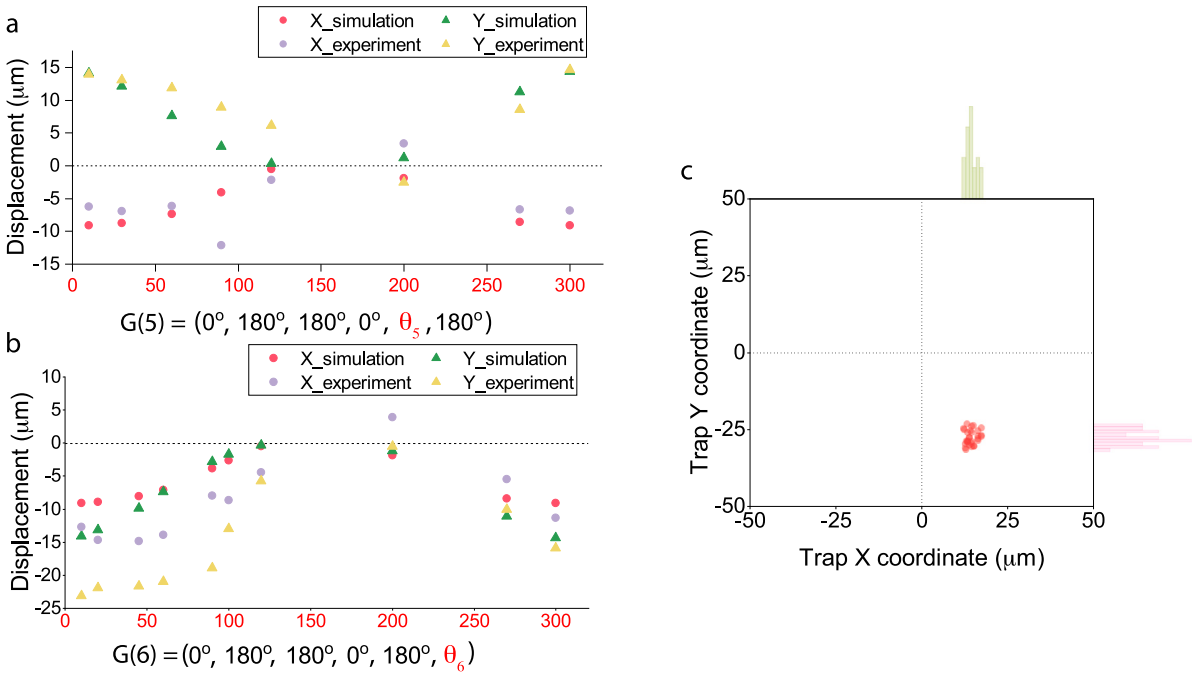

Fig. 7. (a) The comparison of the (x, y) coordinate points of the traps for simulation and experiments for different phase combinations. The results are shown for phase patterns $G(5) = (0°, 180°, 180°, 0°, \theta_5, 180°)$, where θ_5 is the varied from 0° to 300°. (b) The comparison of the (x, y) coordinate points of the traps for simulation and experiments for different phase combinations. The results are shown for phase patterns $G(6) = (0°, 180°, 180°, 0°, 180°, \theta_6)$, where θ_6 is the varied from 0° to 300°. (c) The scatter plot of the (x, y) coordinates of the trapped position when the phase combination of the electrodes was set to $G = (0°, 90°, 180°, 0°, 90°, 180°)$ for 30 repetitions. Histograms indicate the x-axis and y-axis coordinates of the trap location.

Finally, we demonstrate trapping the cell/micro particle at different locations within the trapping zone by varying the phase combinations applied to the six electrodes arranged along the circumference. Fig. 6c shows the GUI with the circular canvas depicting the 100 μm imaging zone and the electrode locations and phases applied to each electrode. The green points in the canvas are the look-up-table (LUT) trap locations whose phase combinations of the electrodes are experimentally verified. The supplementary video S3 shows the user can draw the desired trap locations (drawn as red points in the GUI) and these points are then approximated to the nearest point in the LUT and highlighted in blue sequentially as and when the corresponding phase combination is applied to the electrodes. Fig. 6c shows the six locations defined by the user to trap the cells. The bacteria are then moved to these locations as shown in the snapshots taken from the supplementary video (S3). Four of the six trap positions are shown in Fig. 6c. The supplementary video (S3) was recorded when the six electrodes were applied a frequency of 200 kHz and a voltage of 18 V_{pp} for different phase combinations.

The experimental characterization of the trap positions and comparison with the COMSOL simulations are shown in Fig. 7. The frequency and the applied voltage used in these experiments were 200 kHz and 9 V_{pp}, respectively. Fig. 7a and Fig. 7b show the trend in the x and y positions of the trapped cells in simulation and experiments for two different families of phase combinations: $G(5)$ = (0°, 180°, 180°, 0°, θ_5, 180°) and $G(6)$ = (0°, 180°, 180°, 0°, 180°, θ_6) respectively, where θ_5 and θ_6 are varied from 0° to 300°. The plots show that the trends of the x and y-axis coordinates of the trapped cells in COMSOL simulation (and the neural network which is not shown in the plots as they follow the COMSOL simulations) and the experimental results are similar. Supplementary Figure A3 shows the acquired images of single cyanobacterium captured for θ_5 values of 180°, 120°, 90° *and* 10°, in the phase combination $G(5) = (0°, 180°, 180°, 0°, \theta_5, 180°)$ reported in Fig. 7a. However, the variation in the exact position for each phase combinations could arise due to the difference in the simulation parameters used to model a cell, compared to the actual parameters of the cell. The repeatability of a trap position on application of a specific phase pattern can be observed in Fig. 7c, which shows the variations in the trap positions in the scatter plot as well as the distributions in the x and y-axis coordinates of the trapped cells. The x and y-axis coordinates have a standard deviation of 1.5 μm and 2.3 μm respectively.

4. Conclusion and outlook

In this paper, we have introduced a portable and reconfigurable electronics system (ADEPT) for eDEP applications. This system is capable of generating signals to control up to six electrodes simultaneously with independent V_{pp} amplitudes in the range 0.1 V to 20 V, for frequencies in the range 0 MHz to 10 MHz, phase in the range 0° to 360° and offset in the range 0 V to 5 V, as desired by the user and/or required by the application, and is fully compatible with typical optical microscopes. This compact system with a dedicated graphical user interface is easy to use and does not need a skilled person to operate. We demonstrated the capabilities of the electronics system using a six-electrode microfluidic chip loaded with spherical and rod-shaped cells. Cell manipulation operations of electro-rotation, negative and positive dielectrophoresis and positional trapping were demonstrated. The graphical user interface allows the user to drag microorganisms or particles along a trajectory by drawing the path in a canvas. Simulation studies were employed to identify the trap locations for a phase condition and further extended to neural network model to predict the locations for a given arbitrary phase combination applied to the electrodes. Further regularization during training the deep learning model should support learning the patterns. Additional experiments with encoder–decoder architectures indicated that the inverse problem (from position to phases) could also be solved, thus allowing to predict the original problem (phases to position) with the same model. The established instrument opens up a plethora of applications by simply connecting it to a chip with user-definable electrode designs, while operating the chip in the light path of a suitable microscope.

CRediT authorship contribution statement

Lourdes Albina Nirupa Julius: Conceptualization, Methodology, Data curation, Formal analysis, Writing – original draft, Writing – revision of the manuscript. **Henrik Scheidt:** Methodology, Data curation. **Gowri Krishnan:** Data curation, Formal analysis. **Moritz Becker:** Methodology, Formal analysis, Writing – original draft. **Omar Nassar:** Methodology, Writing – revision of the manuscript. **Sarai M. Torres-Delgado:** Methodology, Writing – revision of the manuscript. **Dario Mager:** Electronics, Writing – revision of the manuscript. **Vlad Badilita:** Methodology, Project administration, Supervision, Writing – revision of the manuscript. **Jan G. Korvink:** Conceptualization, Methodology, Funding acquisition, Project administration, Supervision, Writing – revision of the manuscript.

Declaration of competing interest

The authors declare that they have no known competing financial interests or personal relationships that could have appeared to influence the work reported in this paper.

Data availability

Data will be made available on request.

Acknowledgments

The authors would like to sincerely thank Prof. Annegret Wilde and Dr. Nils Schuergers for access to a Nikon microscope used for the initial experiments, and also for supplying the cells and the DEP buffer used in the experiments and the useful discussion regarding cell handling. The authors would like to thank Dr. Gen Enomoto for supplying the Thermosynechococcus cells. L.A.N.J. and J.G.K. sincerely thank the Deutsche Forschungsgemeinschaft, Germany for funding via project 390131350. The photographs in Fig. 2 were kindly taken by Mr. Amadeus Bramsiepe, Allgemeine Services (AServ), Karlsruhe Institute of Technology (KIT). All authors acknowledge the support of the Karlsruhe Institute of Technology (KIT), also through its publications fund, for providing the infrastructure to realize this work, and for a safe environment during the Covid-19 pandemic.

Appendix A. Supplementary data

Supplementary material related to this article can be found online at https://doi.org/10.1016/j.biosx.2023.100333. The electronics PCB schematic design and layout files of the DEP control hardware along with the software files can be found at the github link: https://github.com/on6315/ADEPT_DEP_Module.git.

References

Bangare, S.L., Dubal, A., Bangare, P.S., Patil, S., 2015. Reviewing Otsu's method for image thresholding. Int. J. Appl. Eng. Res. 10 (9), 21777–21783.

Braschler, T., Demierre, N., Nascimento, E., Silva, T., Oliva, A.G., Renaud, P., 2008. Continuous separation of cells by balanced dielectrophoretic forces at multiple frequencies. Lab Chip 8 (2), 280–286.

Burgarella, S., Merlo, S., Figliuzzi, M., Remuzzi, A., 2013. Isolation of L angerhans islets by dielectrophoresis. Electrophoresis 34 (7), 1068–1075.

Çetin, B., Li, D., 2011. Dielectrophoresis in microfluidics technology. Electrophoresis 32 (18), 2410–2427.

Delgado, S.M.T., Korvink, J.G., Mager, D., 2018. The eload platform endows centrifugal microfluidics with on-disc power and communication. Biosens. Bioelectron. 117, 464–473.

Halfmann, H., Emeis, C., Zimmermann, U., 1983. Electro-fusion of haploid Saccharomyces yeast cells of identical mating type. Arch. Microbiol. 134 (1), 1–4.

Han, S.I., Joo, Y.D., Han, K.H., 2013. An electrorotation technique for measuring the dielectric properties of cells with simultaneous use of negative quadrupolar dielectrophoresis and electrorotation. Analyst 138 (5), 1529–1537.

Huang, L., He, W., Wang, W., 2019. A cell electro-rotation micro-device using polarized cells as electrodes. Electrophoresis 40 (5), 784–791.

Hunt, T.P., Issadore, D., Westervelt, R.M., 2008. Integrated circuit/microfluidic chip to programmably trap and move cells and droplets with dielectrophoresis. Lab Chip 8 (1), 81–87.

Issadore, D., Franke, T., Brown, K.A., Westervelt, R.M., 2010. A microfluidic microprocessor: controlling biomimetic containers and cells using hybrid integrated circuit/microfluidic chips. Lab Chip 10 (21), 2937–2943.

Jen, C.P., Chang, H.H., 2011. Handheld device for the enrichment of rare cells utilising dielectrophoresis in stepping electric fields. Micro Nano Lett. 6 (4), 201–204.

LeCun, Y., Bengio, Y., Hinton, G., 2015. Deep learning. Nature 521 (7553), 436–444.

Liaw, R., Liang, E., Nishihara, R., Moritz, P., Gonzalez, J.E., Stoica, I., 2018. Tune: A research platform for distributed model selection and training. arXiv preprint arXiv:1807.05118.

Manaresi, N., Romani, A., Medoro, G., Altomare, L., Leonardi, A., Tartagni, M., Guerrieri, R., 2003. A CMOS chip for individual cell manipulation and detection. IEEE J. Solid-State Circuits 38 (12), 2297–2305.

Manczak, R., Saada, S., Tanori, M., Casciati, A., Dalmay, C., Bessette, B., Begaud, G., Battu, S., Blondy, P., Jauberteau, M.O., et al., 2018. High-frequency dielectrophoresis characterization of differentiated vs undifferentiated medulloblastoma cells. In: 2018 EMF-Med 1st World Conference on Biomedical Applications of Electromagnetic Fields (EMF-Med). IEEE, pp. 1–2.

Matias, T., Souza, F., Araújo, R., Antunes, C.H., 2014. Learning of a single-hidden layer feedforward neural network using an optimized extreme learning machine. Neurocomputing 129, 428–436.

Nair, V., Hinton, G.E., 2010. Rectified linear units improve restricted boltzmann machines. In: Icml.

Park, K., Suk, H.J., Akin, D., Bashir, R., 2009. Dielectrophoresis-based cell manipulation using electrodes on a reusable printed circuit board. Lab Chip 9 (15), 2224–2229.

Paszke, A., Gross, S., Massa, F., Lerer, A., Bradbury, J., Chanan, G., Killeen, T., Lin, Z., Gimelshein, N., Antiga, L., et al., 2019. Pytorch: An imperative style, high-performance deep learning library. Adv. Neural Inf. Process. Syst. 32.

Pohl, H.A., Hawk, I., 1966. Separation of living and dead cells by dielectrophoresis. Science 152 (3722), 647–649.

Qiao, W., Cho, G., Lo, Y.H., 2011. Wirelessly powered microfluidic dielectrophoresis devices using printable RF circuits. Lab Chip 11 (6), 1074–1080.

Ramirez-Murillo, C.J., de los Santos-Ramirez, J.M., Perez-Gonzalez, V.H., 2021. Toward low-voltage dielectrophoresis-based microfluidic systems: A review. Electrophoresis 42 (5), 565–587.

RoyChaudhuri, C., Das, R.D., Dey, S., Das, S., 2011. Functionalised silicon microchannel immunosensor with portable electronic readout for bacteria detection in blood. In: SENSORS, 2011 IEEE. IEEE, pp. 323–326.

Samanta, N., Kundu, O., Chaudhuri, C.R., 2013. A simple low power electronic readout for rapid bacteria detection with impedance biosensor. IEEE Sens. J. 13 (12), 4716–4724.

Sarno, B., Heineck, D., Heller, M.J., Ibsen, S.D., 2021. Dielectrophoresis: Developments and applications from 2010 to 2020. Electrophoresis 42 (5), 539–564.

Trainito, C.I., Sweeney, D.C., Čemažar, J., Schmelz, E.M., Français, O., Le Pioufle, B., Davalos, R.V., 2019. Characterization of sequentially-staged cancer cells using electrorotation. PLoS One 14 (9), e0222289.

Van Rossum, G., Drake, F.L., 2009. Python 3 Reference Manual. CreateSpace, Scotts Valley, CA.

Wolfram Research, Inc., 2021. Mathematica, version 13.0.0. URL: https://www.wolfram.com/mathematica. Champaign, IL.

Yang, J., Zhao, L.P., Yin, Z.Q., Hu, N., Chen, J., Li, T.Y., Svir, I., Zheng, X.L., 2010. Chip-based cell electrofusion. Adv. Eng. Mater. 12 (9), B398–B405.

Zhang, H., Chang, H., Neuzil, P., 2019. DEP-on-a-chip: Dielectrophoresis applied to microfluidic platforms. Micromachines 10 (6), 423.

Ziyin, L., Hartwig, T., Ueda, M., 2020. Neural networks fail to learn periodic functions and how to fix it. Adv. Neural Inf. Process. Syst. 33, 1583–1594.